



HAL
open science

Wire mesh stack and regenerator model for thermoacoustic devices

Elio Di Giulio, Cong Truc Nguyen, Camille Perrot, Raffaele Dragonetti

► **To cite this version:**

Elio Di Giulio, Cong Truc Nguyen, Camille Perrot, Raffaele Dragonetti. Wire mesh stack and regenerator model for thermoacoustic devices. *Applied Thermal Engineering*, 2023, 221, pp.119816. 10.1016/j.applthermaleng.2022.119816 . hal-04121509

HAL Id: hal-04121509

<https://hal.science/hal-04121509>

Submitted on 13 May 2024

HAL is a multi-disciplinary open access archive for the deposit and dissemination of scientific research documents, whether they are published or not. The documents may come from teaching and research institutions in France or abroad, or from public or private research centers.

L'archive ouverte pluridisciplinaire **HAL**, est destinée au dépôt et à la diffusion de documents scientifiques de niveau recherche, publiés ou non, émanant des établissements d'enseignement et de recherche français ou étrangers, des laboratoires publics ou privés.

WIRE MESH STACK AND REGENERATOR MODEL FOR THERMOACOUSTIC DEVICES

Elio Di Giulio^{1,*}, Cong Truc Nguyen², Camille Perrot², Raffaele Dragonetti¹

¹*Department of Industrial Engineering, University of Naples Federico II, 80125 Naples, Italy.*

²*Univ Gustave Eiffel, Univ Paris Est Creteil, CNRS, UMR 8208, MSME, F-77454 Marne-la-Vallée, France*

*Corresponding author: elio.digiulio@unina.it

Keywords: *wire mesh, stack, thermoacoustics, thermoviscous functions, transport parameters.*

ABSTRACT

Thermoacoustic technology can play a significant role in the development of renewable energies. Thermoacoustic engines and heat pumps (or refrigerators) are however characterized by a low efficiency attributed to suboptimal components. The core of these devices is a porous material, named stack (or regenerator), in which thermoacoustic conversion takes place. The most frequently used stack in the literature remains the wire mesh, although there is still a lack of formulation for the corresponding thermoviscous response functions. Essentially, all the dynamic thermal and viscous behaviors of a porous structure can be derived thanks to the Johnson-Champoux-Allard-Lafarge (JCAL) semi-phenomenological model, where transport parameters provide input information on the macroscopic level to the model. Here, we report a set of structure-property correlations between the transport parameters of the stack and the geometrical features of the wire mesh obtained from first-principles calculations. Validation of the model is carried out by means of experimental measurements performed on three different specimens. Our results show that the knowledge of the thermoviscous functions for the wire mesh allows drawing preliminary considerations on the thermoacoustic efficiency of the stack, without needing to consider a full numerical simulation of the entire device.

efficiency of these devices means to better understand the phenomena which occur in that porous core and then to find the optimal geometry for each specific case. The literature shows that thermoacoustic technologies have been used in different applications such as electricity generation [3–5], domestic refrigeration [6,7], automotive industry [8], cryogenics [9], and thermal management of electronic devices [10,11].

In these applications, wire meshes (or stacked screen bed) are largely used, because they are easy to realize with respect to other classical uniform cross-sectional stacks (parallel plates, circular pores and pin array); and they offer a low ratio between the fluid volume and the fluid-solid interface area which makes them suitable for travelling wave devices [8,12–17]. There is, however, a lack of an accurate model in the literature to describe the viscous and thermal properties of this kind of stacks. The performance predictions of a stack are usually determined from semi-empirical correlations provided by Swift and Ward [18]. They are, however, restricted to a specific geometrical configuration in their current form --which limits their ability to study how thermoacoustic efficiency relates to the geometrical details of the wire mesh stack.

This paper is therefore devoted to the derivation of a more general model, linking wire mesh geometrical descriptors to classical thermoviscous functions f_v and f_k , as available in the literature for standard uniform cross section stacks [19]. The knowledge of the visco-thermal behaviour as a function of the geometrical parameters of wire mesh (e. g., the radius of the struts r_p and the step between the struts p ; see Fig. 1) would offer the ability to find directly the optimal geometrical parameters for each specific application of interest, based on the other thermoacoustic device parameters (such as the working frequency, the length of the resonator, the hot and cold temperatures). Since the Johnson-Champoux-Allard-Lafarge (JCAL) [20–22] semi-phenomenological model conveniently describes the dynamic complex viscous and thermal behaviour of porous materials [23,24] at macro-scale from the knowledge of six transport parameters, the idea is to numerically solve the partial differential equations governing these macroscopic transport properties in the studied geometry; and then to provide detailed quantitative correlations of how transport parameters vary with geometrical descriptors.

In the Sec. II, the theoretical background is introduced with a brief review of the viscous f_v and thermal f_k functions of the porous material, in addition to providing their dependency on the six transport parameters of the JCAL model. In Sec. III, we then describe the geometrical model through which we simulate the flow, and the corresponding numerical computations leading to the transport parameters. Our present results linking geometrical parameters of the wire mesh with the transport parameters of the stacks are reported in Sec. IV, together with an analytical formulation of the heat capacity ratio accounting for the imperfect isothermal condition at the fluid-solid interface. A validation of the method is presented through the comparison of the calculated thermoviscous functions with laboratory measurements in Sec. V. Finally, a few remarks conclude this work.

II. THEORETICAL BACKGROUND

From a theoretical point of view, the dynamic viscous and thermal behaviour of a generic porous material under the action of an oscillating flow (with angular frequency $\omega = 2\pi f$, and f the frequency) can be derived by solving three linearized equations: continuity, momentum and energy coupled with the equation of state in the frequency domain. Considering the mean values of the thermodynamic quantities (p_m, T_m) as being constant and assuming that the mean value of the velocity is zero, that is $\mathbf{v}_m = \mathbf{0}$ (non-convective effects); pressure, temperature, and particle velocity can be written as:

$$p = p_m + \Re[p_1 e^{i\omega t}] \quad (1)$$

$$T = T_m + \Re[T_1 e^{i\omega t}] \quad (2)$$

$$u = \Re[u_1 e^{i\omega t}] \quad (3)$$

where p_1 is the acoustic pressure, T_1 the excess oscillating temperature, u (and u_1) is the projection of acoustic velocity vector \mathbf{v} along the wave propagation direction, $e^{i\omega t}$ is the complex time factor, $i = \sqrt{-1}$ is the imaginary unit and \Re represents the real part of a complex number. Under scale separation between the wavelength and the characteristic size of the pore (as highlighted by Kirchhoff [25] for $r_w f^{3/2} < 10^6 \text{ cm s}^{-3/2}$, with r_w the tube radii being greater than 10^{-3} cm), momentum and energy equations allow to describe the visco-inertial and heat diffusion effects separately [26, 27]:

$$i\omega\rho_m u_1 = -\nabla p_1 + \mu\nabla^2 u_1, \quad (4)$$

$$i\omega\rho_m c_p T_1 = i\omega p_1 + \kappa\nabla^2 T_1; \quad (5)$$

ρ_m is the equilibrium density of air, μ, κ and c_p are respectively the dynamic viscosity, the thermal conductivity and the specific heat at constant pressure of air. Under the hypothesis of rigid and isothermal walls ($u_1(\text{wall}) = 0, T_1(\text{wall}) = 0$) of the material solid skeleton, space-averaged solutions of Eqs. (4)-(5) can be written in terms of two frequency-dependent response-functions introduced by Zwikker and Kosten [28] to describe the overall acoustic behaviour of fluid saturated porous materials: the complex density $\tilde{\rho}(\omega)$ and bulk modulus $\tilde{K}(\omega)$.

In thermoacoustics, a static temperature gradient along the material, dT_m/dx , is artificially added by means of a hot and a cold heat exchanger. In this case the temperature field across the material is written as

$$T(x) = T_m(x) + \Re[T_1 e^{i\omega t}]. \quad (6)$$

Taking into account Eq. (6), Eq. (5) becomes,

$$i\omega\rho_m c_p T_1 + \rho_m c_p \frac{dT_m}{dx} u_1 = i\omega p_1 + \kappa\nabla^2 T_1. \quad (7)$$

Complex density and bulk modulus are obviously intrinsic properties of the material, which do not change when the thermal gradient is applied. In thermoacoustics, thermoviscous functions f_v and f_κ are generally used to describe the dynamic behaviour of the porous

media. These functions are strictly linked to the aforementioned complex density and bulk modulus, as shown by Dragonetti *et al.* [29]:

$$\tilde{\rho} = \frac{\rho_m}{1 - f_v}, \quad (8)$$

$$\tilde{K} = \frac{\gamma p_m}{1 + (\gamma - 1)f_\kappa}. \quad (9)$$

For porous materials with simple geometrical shapes, such as uniform cross section (parallel plates, circular pores, pin array), thermoviscous functions (or, equivalently, complex density and bulk modulus) are expressed from analytical relations depending only on the geometrical factors of the system (semi-distance between plates, radius of circular pore, diameter of pin). In the case of complex porous media such as fibrous, granular and foam materials, the dynamic visco-thermal behaviour can be assessed through the Johnson-Champoux-Allard-Lafarge (JCAL) semi-phenomenological model. This model requires six input parameters (termed *transport parameters*) which are related to geometrical quantities of the microstructure representing the porous material. The six transport parameters of the JCAL model are: the porosity ϕ , the thermal Λ' and viscous Λ characteristic lengths, the tortuosity α_∞ , the static viscous k_0 and thermal k'_0 permeabilities. A definition of these transport parameters will be given in Sec. III. Once these parameters are known, the dynamic frequency-dependent visco-thermal properties can be expressed by combining the JCAL model with the Dragonetti *et al.* relations, Eqs. (8)-(9), as follows:

$$f_v = 1 - \frac{1}{\alpha_\infty \left(1 + \frac{\phi \mu}{i \omega \rho_m k_0 \alpha_\infty} \sqrt{1 + i \frac{4 \alpha_\infty^2 k_0^2 \rho_m \omega}{\phi^2 \mu \Lambda^2}} \right)}, \quad (10)$$

$$f_\kappa = 1 - \frac{1}{1 + \frac{\phi \kappa}{i k'_0 c_p \omega \rho_m} \sqrt{1 + i \frac{4 k'_0{}^2 c_p \rho_m \omega}{\kappa \Lambda'^2 \phi^2}}}. \quad (11)$$

Wire mesh, also named stacked screen (Fig. 1), was applied for the first time in thermoacoustics by Swift and Ward [18]. In their work, these authors introduced the possibility to use this kind of material as a porous core in thermoacoustic devices. In particular, wire mesh seemed to be suitable as a regenerator in travelling wave devices, where very small $r_h/\delta_{v(\kappa)}$ ratio are required; here $r_h = 2A/p_{wet}$ is the hydraulic radius defined as the ratio between the cross-sectional area A and the wet perimeter p_{wet} , and $\delta_v = \sqrt{2\mu/\omega\rho_m}$ ($\delta_\kappa = \sqrt{2\kappa/\omega\rho_m c_p}$) is the viscous (resp. thermal) boundary layer. General analytical solutions of Eqs. (4) and (5) do not exist, this is also the case for wire mesh geometries. For this reason, Swift and Ward [18] proposed a description of the dynamic viscous and thermal-relaxation effects of these materials from the friction factor and heat transfer data of Kays and London [30], derived from a steady-state assumption:

$$\frac{dp_1}{dx} = -i\omega\rho_m \left[1 + \frac{(1-\varphi)^2}{2(2\varphi-1)} \right] \langle u_1 \rangle - \frac{\mu}{r_h^2} \left(\frac{c_1(\varphi)}{8} + \frac{c_2(\varphi)R_{e,1}}{3\pi} \right) \langle u_1 \rangle, \quad (12)$$

$$\begin{aligned} \frac{d\langle u_1 \rangle}{dx} = & -\frac{i\omega}{\gamma p_m} p_1 + \frac{1}{T_m} \frac{dT_m}{dx} \langle u_1 \rangle + \\ & + \frac{i\omega}{T_m} \left[\frac{1}{\rho_m c_p} \frac{(g_c + e^{2i\theta_p} g_v) \varepsilon_h}{1 + \varepsilon_h (g_c + e^{2i\theta_T} g_v)} p_1 - \frac{1}{i\omega} \frac{dT_m}{dx} \frac{(g_c - g_v) \varepsilon_h}{1 + (g_c + e^{2i\theta_T} g_v) \varepsilon_h} \langle u_1 \rangle \right]; \end{aligned} \quad (13)$$

where $R_{e,1} = 4|\langle u_1 \rangle| r_h \rho_m / \mu$ is the complex Reynolds-number amplitude, and the angular brackets $\langle \ \rangle$ represent a cross-sectional average. θ_p and θ_T are respectively the phase angle between the oscillating velocity and pressure and oscillating velocity and temperature. $c_1(\varphi)$, $c_2(\varphi)$ and ε_h are polynomial correlations expressed as functions of porosity, while g_c and g_v can be assessed from trigonometric integrals. More details are reported in [31].

All these elements make heavy and tedious the general description of the visco-thermal behavior of such materials. Therefore, it would be desirable to extend the simple use of thermoviscous functions, f_v and f_k , to a convenient analytical formulation, as available for other canonical geometries (parallel plates, circular pores, pin arrays). Because f_v and f_k are intrinsic properties of the materials; the possibility to characterize the thermo-viscous functions for the wire mesh would allow making preliminary considerations on the behavior of these materials and then on their thermo-acoustic efficiency without simulating the entire device.

The JCAL model can be employed to assess the thermoviscous functions for each porous materials under oscillating flows. In that case, the characterization of a material depends on the knowledge of six transport parameters. These intrinsic parameters can be assessed by means of numerical simulations, once the microstructure of the material is known.

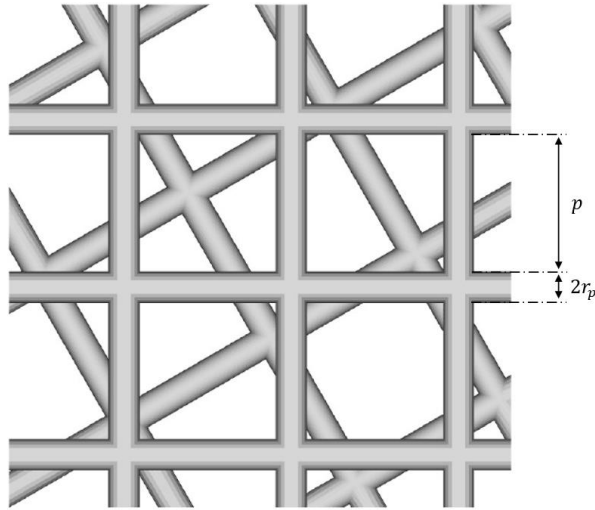


Figure 1. Schematic representation of the wire mesh stack and its geometrical descriptors.

III. NUMERICAL APPROACH

Linearized continuity, momentum and energy equations allow to solve the thermofluid dynamic fields inside the porous materials under oscillating flow conditions. The homogenization theory [32] highlights that when a scale separation exists, viscous and thermal effects can be decoupled. In particular, thanks to the JCAL model, the knowledge of the dynamic complex behaviour of the material is a function of only six non-acoustical parameters, which can be assessed from three boundary value problems [33–37]. Wire meshes are practically obtained through superposition of several layers of grid, placed in a random way. The basic physics corresponding to the different simulations are as follows.

- Firstly, solving the *Stokes flow*, leads to the assessment of the static viscous permeability k_0 of the porous structure under study. For low Reynolds number flow hydrodynamics, corresponding to an incompressible Newtonian fluid,

$$k_0 = \varphi \frac{\langle u \rangle}{\Delta p / D_t}, \quad (14)$$

where $\langle u \rangle$ is the average velocity over the fluid phase, Δp the applied pressure difference and D_t is the size of the unit cell.

- Secondly, a resolution of the *Laplace problem* enables the assessment the high-frequency parameters derived in the case of an inviscid ideal fluid: the tortuosity α_∞ and the viscous characteristic length Λ . According to the electrical conduction analogy [20, 38], once an electric potential difference ΔV is applied across the unit cell in which the solid phase is insulating and the saturating fluid is conductive, the parameters can be estimated as

$$\alpha_\infty = \frac{\langle E \cdot E \rangle_{V_f}}{\langle E \rangle_{V_f} \cdot \langle E \rangle_{V_f}}, \quad (15)$$

$$\Lambda = \frac{2 \int_{V_f} E \cdot E dV_f}{\int_{A_{fs}} E \cdot E dA_{fs}}; \quad (16)$$

where V_f and A_{fs} denote, respectively, the fluid volume and the fluid surface area of the pore space, E is the local electric field deriving from a scalar potential, the scalar potential being itself the solution of the Laplace problem.

- Third, finding the solution of the *Poisson problem* provides us with a means to assess the static thermal permeability, k'_0 , as

$$k'_0 = \varphi \langle \tau \rangle_{V_f}; \quad (17)$$

where τ is the scaled temperature field which solves Poisson's equation inside the unit-cell,

$$\nabla^2 \tau = -1. \quad (18)$$

Porosity φ and thermal characteristic length Λ' are geometrical parameters that can be evaluated directly from the unit-cell:

$$\varphi = \frac{V_f}{V_{total}}, \quad (19)$$

$$\Lambda' = \frac{2 \int_{V_f} dV_f}{\int_{A_{fs}} dA_{fs}}, \quad (20)$$

with V_{total} the total volume of the unit cell including both the solid and fluid fractions. Periodic boundary conditions were applied through the thickness by imposing continuity of the microscopic velocity field while the lateral boundaries were subjected to continuity of the microscopic pressure field.

It was observed, from the numerical procedure reported throughout Appendix A, that the relative error of both the viscous and thermal permeability computations between two subsequent calculations corresponding to the number n of grid layers, was typically less than 5 %, for $n = 6$. The maximum relative differences for the other transport parameters were less than 1%. The Representative Volume Element (RVE) was therefore considered in this study to be composed of six superimposed grid layers (Fig. 2).

Lateral dimensions were imposed to be twice those of the thickness. Under these circumstances, it was observed that the lateral dimensions have no influence on the results when increasing their size.

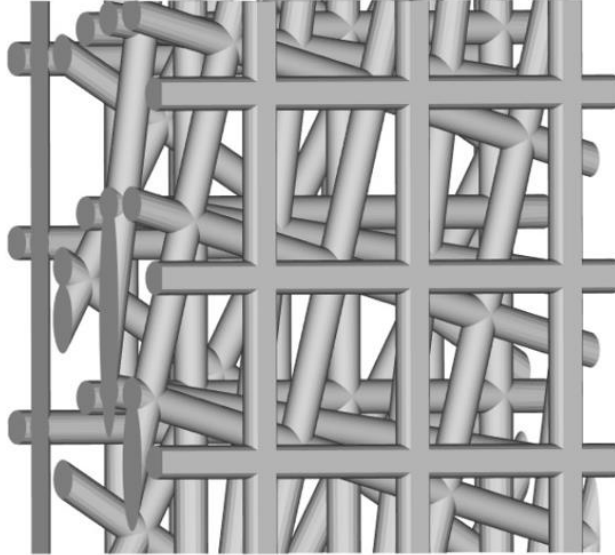


Figure 2 : An illustrative example of wire mesh stack representative volume element. For the sake of clarity, only the solid skeleton of the wire mesh stack of through-thickness D_t is displayed.

IV. SIMULATION RESULTS AND DERIVATION OF THE MODEL

Simulations were carried out on 150 different unit-cells obtained by varying the strut radius r_p from 0.13 to 0.78 mm, and the distance between struts d_s from 1 to 3.5 mm. Note that this range of variations of r_p and d_s parameters encompasses the typical dimensions of commercial wire screens [13-14]. It is also noteworthy that the geometry of wire mesh is characterized by intertwined metal filaments, while we constructed a simplified model of the wire mesh. The junction at two connected filaments was represented as a straight intersection. This model was found to be accurate enough for the prediction of the transport parameters of wire mesh stacks (Appendix A).

Through Eqs. (14)-(20), transport parameters were evaluated for each unit-cell. Subsequently, the general structure of the proposed correlations between geometrical descriptors and transport parameters was inspired from the ones provided by Luu *et al.* [39]. This was possible because of the similarity between wire mesh and fibrous structure. The proposed correlations are summarized in Tab. I, together with some statistical indicators assessing the goodness-of-fit. A systematic quantitative appreciation of the adequacy of the fitted model was also performed through residuals analysis and reported in Appendix B.

Table I. Transport parameters' correlations for wire mesh stacks. R-squared is the coefficient of determination, while SSE denotes the sum squared errors of residuals.

Parameter	Correlation	R-squared	SSE
Porosity	$\varphi = 1 - 0.7099 \frac{\pi r_p}{d_s + 2r_p}$	0.9806	0.0493
Thermal Characteristic Length	$\frac{\Lambda'}{r_p} = \frac{\varphi}{1 - \varphi - 0.005133}$	0.9845	10.38
Viscous Characteristic Length	$\frac{\Lambda}{r_p} = 0.4825 \frac{\varphi}{1 - \varphi + 0.04564}$	0.9802	1.284
Tortuosity	$\alpha_\infty = \left(\frac{1}{\varphi}\right)^{0.5807}$	0.9657	0.1303
Static Viscous Permeability	$\log_{10} \left(\frac{k_0}{r_p^2}\right) = 0.7765 \log_{10} \left(\frac{\varphi^3}{(1 - \varphi)^2}\right) - 0.9855$	0.9993	0.0605
Static Thermal Permeability	$\log_{10} \left(\frac{k'_0}{r_p^2}\right) = 0.7258 \log_{10} \left(\frac{\varphi^3}{(1 - \varphi + 0.3054)^2}\right) - 0.6741$	0.9992	0.1802

To complete the thermoacoustic description of a porous material, the heat capacity ratio ε_s parameter [2] is needed in order to take into account the imperfect isothermal condition provided by the solid matrix. Implicitly, Eq. (5) is solved in the case of an isothermal solid condition, meaning that a Dirichlet boundary condition is applied at the fluid-solid interface ($T_1 = 0$). In practical situations however, due to the variation of temperature, both fluid and solid thermal properties may evolve, and the most appropriate boundary condition for the energy equation is the Robin boundary condition as reported in [40],

$$T_{1,fluid} = T_{1,solid} \quad \kappa \nabla T_{1,fluid} = -\kappa_s \nabla T_{1,solid}; \quad (21)$$

where κ_s is the thermal conductivity of the solid matrix. Note that the subscript 1 indicates here that the solid matrix can no more act as a thermostat imposing its temperature. The heat capacity ratio ε_s allows to express how far the solid skeleton is from an isothermal condition. This parameter turns out to be equal to zero for a perfect isothermal solid condition and tends towards infinity in the case of an adiabatic condition. ε_s can be assessed in an operative way as follows,

$$\varepsilon_s = \frac{\rho_m c_p f_\kappa}{\rho_s c_s f_s} \frac{\varphi}{1 - \varphi}, \quad (22)$$

where ρ_s and c_s are, respectively, the density and the heat capacity of the solid material and f_s is the dynamic thermal function (a solid dynamic thermal function understood as an analogue to f_κ for the fluid part) depending only on the geometry of the solid structure.

Therefore, the dynamic thermal function f_s is the only missing parameter to assess the heat capacity ratio ε_s and fulfil the overall thermoacoustic description of the stacks. In the case of a wire mesh, the solid structure geometry can be considered as an array of circular rods, for which an analytical formulation of the solid thermal function exists,

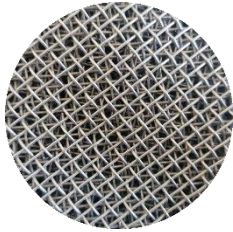


$$f_s = 2 \frac{J_1[(i-1)r_p/\delta_s]}{J_0[(i-1)r_p/\delta_s]}, \quad (23)$$

where $\delta_s = \sqrt{2\kappa_s/\omega\rho_s c_s}$ is the thermal boundary layer inside the solid medium and J_1, J_0 are respectively the Bessel's functions of first and zero order.

V. EXPERIMENTAL RESULTS

Three different wire mesh specimens have been realized and tested to validate the proposed transport parameter models. Geometrical data of the experimental samples are reported in Tab. II.

Table II. Geometrical data of the wire mesh samples.

Sample		Radius of the struts r_p [mm]	Step between the struts d_s [mm]
Wire Mesh 1		0.35	3.07
Wire Mesh 2		0.30	2.30
Wire Mesh 3		0.20	1.63

In the literature, different experimental methodologies were applied to characterize the dynamic viscous and thermal properties of porous materials. The most commonly used experimental setups are the three-[41] and four-[42] microphones impedance tube techniques. Other measurement methods, specific to low frequency stimuli, such as in thermo-acoustics, are the lumped element techniques [43–46]. Note that in thermo-acoustics, the stack works primarily at frequencies below 500 Hz. For this reason, the low frequency acoustic methods presented in [45–46] were employed to characterize the viscous and thermal behaviours of the three wire mesh samples under study. This methodology requires the use of two single microphones, to measure the pressure in the cavity where the sample is placed and the pressure behind the loudspeaker. For the assessment of the viscous behavior, the sample is placed between the loudspeaker membrane and an open-end, while for the thermal behavior a rigid termination is placed back onto the specimen. For each test two measurements are required: once with the sample (*full*) and one only with air fulfilling the sample holder (*empty*). The techniques are particularly suitable in low frequency range, where the standard three- and four- microphones methods are limited from the geometrical dimensions of the setup, such as the separation distances between adjacent microphones and the inner diameter of the tube. As a control, the measurement procedure was repeated three times, for each of the considered sample. The reason for performing the measurements three times was to determine the dispersion of experimental data, in particular as a function of frequency.

In agreement with the theoretical background introduced in Sec. II, the experimental results are reported in terms of the viscous and thermal functions, f_v and f_k . Figs. 3-5 compare the experimental results obtained through the lumped element technique with our model combining the JCAL approach with the proposed transport parameter derivations (Tabs. I and II). Plots are reported in terms of the real and imaginary parts of the viscous and thermal functions. Experimental data are generally in good agreement with the theoretical predictions both for the viscous and thermal behaviors. Based on the equations reported in Table I, the estimated values of the viscous $f_{vt} = \mu\phi/(2\pi\rho_0\alpha_\infty k_0)$ and thermal $f_{tt} = \kappa\phi/(2\pi\rho_0 c_p k'_0)$ transition frequencies, for the three wire mesh samples that were characterized (wire mesh 1 to 3), are respectively equal to 19, 32, 65 Hz and 14, 21, 45 Hz. Therefore, most of the measured behaviours of the viscous f_v and thermal f_k functions correspond only to the inertial and adiabatic regimes.

It can be highlighted that experimental data start to deviate from the model prediction when the frequency increases. This is due to a limit in the high frequency range of the lumped element technique, where the validity range of the methodology is function of the sample parameters. Notably, the greater the viscous losses (i.e. the airflow resistivity) the smaller the range of frequencies in which the measurements are valid. In [45–46], the range of frequencies over which the measurements are valid was established for values corresponding to $abs(\tilde{k}d) < 0.5$; where $\tilde{k} = \omega \sqrt{\frac{\rho_m}{\gamma p_m} \frac{1+(\gamma-1)f_k}{1-f_v}}$ is the complex wavenumber

and d is the sample thickness. For the experimental samples under study, the corresponding cut-off frequencies for Wire Mesh 1, 2 and 3 are respectively equal to 535, 521 and 509 Hz.

Some differences between the experimental data and the model were observed for the imaginary part of the thermal response function, f_k (below 50 Hz). This resulted mostly because of difficulties inherent to the measurement technique, which requires a perfectly sealed setup to avoid air losses and an acoustic source able to support the front and rear compliance volumes [45]. In our experimental setup, the used acoustic source was not properly designed to work under such low frequencies. As a consequence, an increasing standard deviation was characterized when the frequency decreases. Specifically, the difference in amplitude between the experimental results and the model predictions for the thermal function f_k of the Wire Mesh 1 (Fig. 3a) resulted mostly from the fact that a larger thermal permeability k'_0 was observed when compared with the other samples (Tab. I and II). In agreement with the previous statement about the thermal transition frequency f_{tt} , the associated transition between the isothermal and adiabatic regimes of 14 Hz indicates that an accurate measurement of both the real and imaginary part of f_k would require a specifically designed experimental setup.

Because the experimental validation of the model is provided under ambient air conditions, the imperfect isothermal condition highlighted through Eqs. (21)-(23) had no impact, and the heat capacity ratio ε_s was clearly set to zero. It is noteworthy that, in classical thermoacoustic applications where the temperature gradients are high and the thermophysical properties of the fluid and the solid matrix make the isothermal condition no more valid, the proposed model is general enough and can be applied including Eqs. (21)-(23).

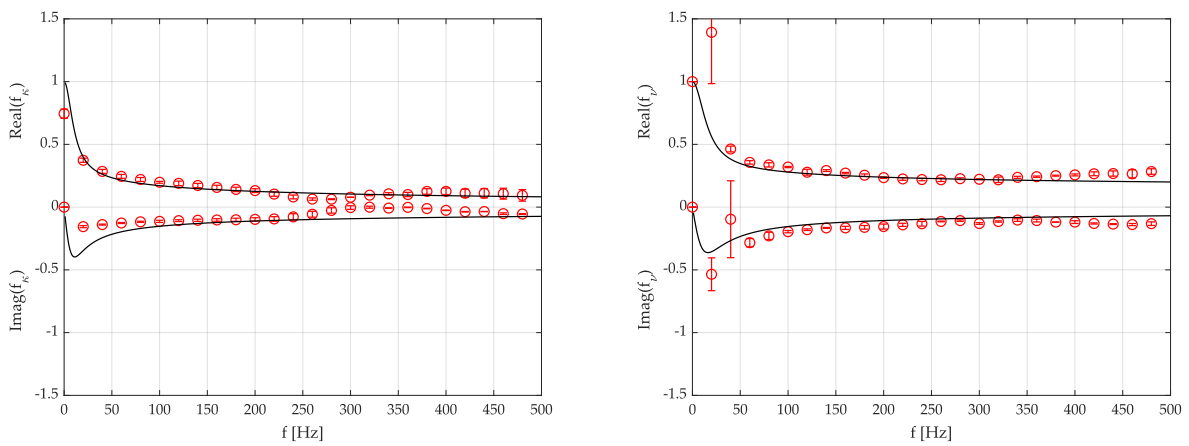


Figure 3. Wire mesh 1: Comparison between experimental results (red circular points, mean value \pm standard deviation) and modelling approach (continuous black line). Real and imaginary parts of the frequency-dependent (a) thermal function f_k and (b) viscous function f_v .

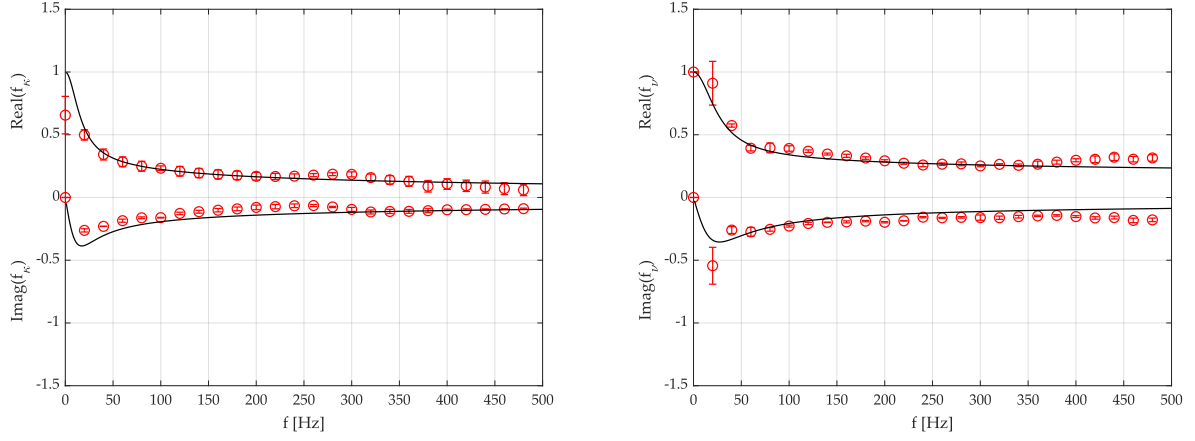


Figure 4. Wire mesh 2: Comparison between experimental results (red circular points, mean value \pm standard deviation) and modelling approach (continuous black line). Real and imaginary parts of the frequency-dependent (a) thermal function f_k and (b) viscous function f_v .

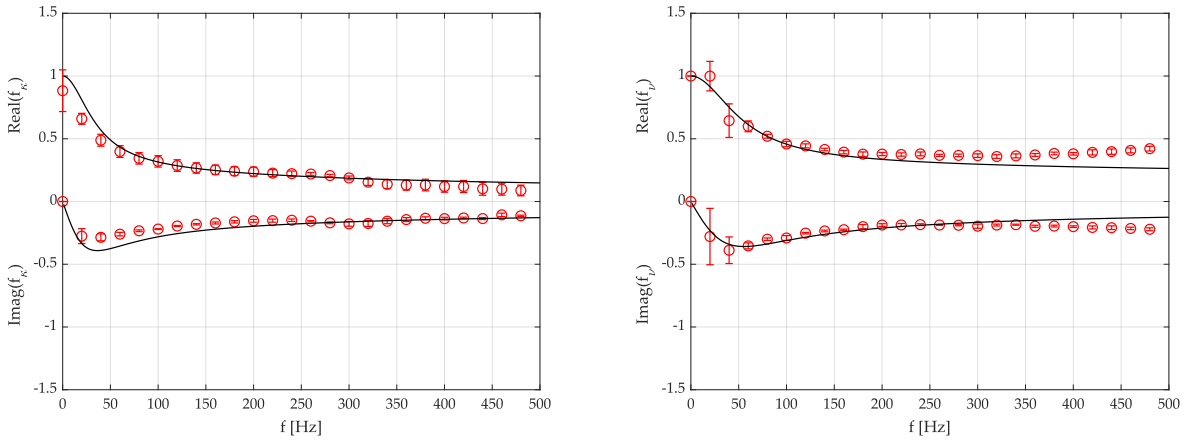


Figure 5. Wire mesh 3: Comparison between experimental results (red circular points, mean value \pm standard deviation) and modelling approach (continuous black line). Real and imaginary parts of the frequency-dependent (a) thermal function f_k and (b) viscous function f_v .

VI. CONCLUSION

In this work, a model to assess the transport parameters of wire mesh stacks is provided as a function of its geometrical descriptors (the radius of the struts, r_p , and the characteristic step between two struts, p). These simple relationships between geometrical and transport parameters allow the use of the JCAL semi-phenomenological model, in order to characterize the dynamic viscous and thermal behavior of the porous system, in terms of two standards f_v and f_k response functions. To further elaborate on the thermoacoustic description of this kind of stacks (regenerators), a complementary formulation of the dynamic thermal function of the solid (and subsequently the heat capacity ratio, ε_s) was also provided. Experimental measurements carried out on three different samples agreed quite well with the proposed model. In conclusion, because all transport parameters of wire mesh stacks can be determined from direct micro-macro relationships (Table I); this procedure makes it possible to obtain simultaneously the intrinsic viscous f_v and thermal f_k frequency-dependent behavior from the geometrical description of the solid constituents

(r_p, d_s) . It is especially well suited to further study the overall performance of thermoacoustic engines, using wire-mesh stacks, which depends on a certain number of operating parameters (working frequencies, stack position, amount of thermal energy to be exchanged, temperature gradient). An innovative method was therefore proposed to derive structure-property relationships, which are extremely useful in the early stages of design of a thermoacoustic engine, because they quickly promptly give the designer quantitative information allowing preliminary assessment of the viscous and thermal dissipative powers inside the stack. In particular, using these relationships should be extremely valuable to properly determine the geometrical parameters of the wire mesh so as to maintain a relatively low amount of viscous effects and increase the thermal ones in order to promote thermal energy exchanges.

ACKNOWLEDGMENTS

This work was partly supported by the Italian Ministry of University and Research (MIUR) under Project number PRIN 2017JP8PHK. The activities of Elio Di Giulio were supported by UniNA and Compagnia di San Paolo, in the framework of Programme STAR PLUS. Elio Di Giulio was on leave at University Gustave Eiffel from October the 1st of 2021 to March the 31st of 2022 thanks to a UNINA-DII fellowship (under the specific agreement between Université Gustave Eiffel and Università degli Studi di Napoli Federico II number 2021/424).

Declaration of Competing Interest: The authors declare no conflict of interest.

Appendix A. Definition of the unit cell used to perform the numerical simulations

Wire meshes are realized by intertwined metal filaments (Figs. 6a and 6b). The geometry of the RVE was simplified by considering intersecting filaments at the junctions (Figs. 6c and 6d).

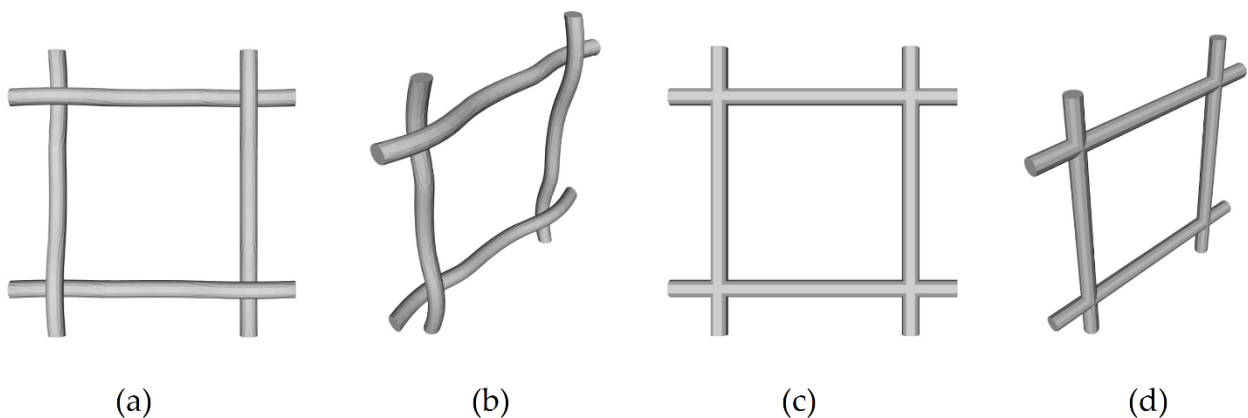


Figure 6. Intertwined metal filaments. [front (a) and perspective (b) views] compared to the simplified model with intersecting filaments [front (c) and perspective (d) views].

The effects of this simplification on the transport parameter values were assessed by means of numerical simulations on a single layer. The relative differences Δ between transport

parameters of intertwined and intersecting filaments was much lower than 5%, with a small exception for the characteristic length (attributed to the lower wetted surface area ratio of the straight pattern); Tab. III. Following this analysis, the simplified geometry was chosen to realize the RVE, mainly for two reasons: (i) the greater simplicity to build the geometry; (ii) this approach allowed us to avoid uncertainties usually associated with the analysis of singular geometrical problems (due to the mesh in the vicinity of critical points, such as the contact of two filaments in the intertwined case).

Table III. Transport parameter values of an intertwined and intersecting wire mesh geometry ($r_p = 0.15 \text{ mm}$, $d_s = 3.3 \text{ mm}$).

	φ [-]	α_∞ [-]	Λ [mm]	Λ' [mm]	k_0 [cm ²]	k'_0 [cm ²]
Intertwined	0.9536	1.0385	0.7936	2.6254	0.2981	0.5115
Intersecting	0.9533	1.0456	0.7596	2.7806	0.2930	0.5199
$\Delta\%$	0.04	0.68	4.49	5.58	1.73	1.60

The representative volume element (RVE) on which the numerical simulations are carried out is based on six superimposed layers, randomly oriented (Fig. 2). The convergence of the transport parameters was assessed by adding progressively supplementary layers of wire-mesh. For a given number of layers, the simulations were repeated four times with the relative orientation of each horizontal layer being chosen randomly. Results are presented as mean \pm standard deviation (Fig. 7). The relative difference Δ between the mean value corresponding to a transport parameter with n layers and the mean value corresponding to the same transport parameter with $n - 1$ layers was found to be less than 1 % for the porosity (Fig. 7a) and for the tortuosity (Fig. 7b), and less than 5 % for the characteristic lengths (Figs. 7c and 7d); with $n = 6$. Considering the viscous k_0 and thermal k'_0 permeabilities, the relative difference declines appreciably with the number of layers, with a relatively stable level for $n \geq 4$ (Figs. 7e and 7f). A value of $n = 6$ represents a good tradeoff between accuracy and computational time.

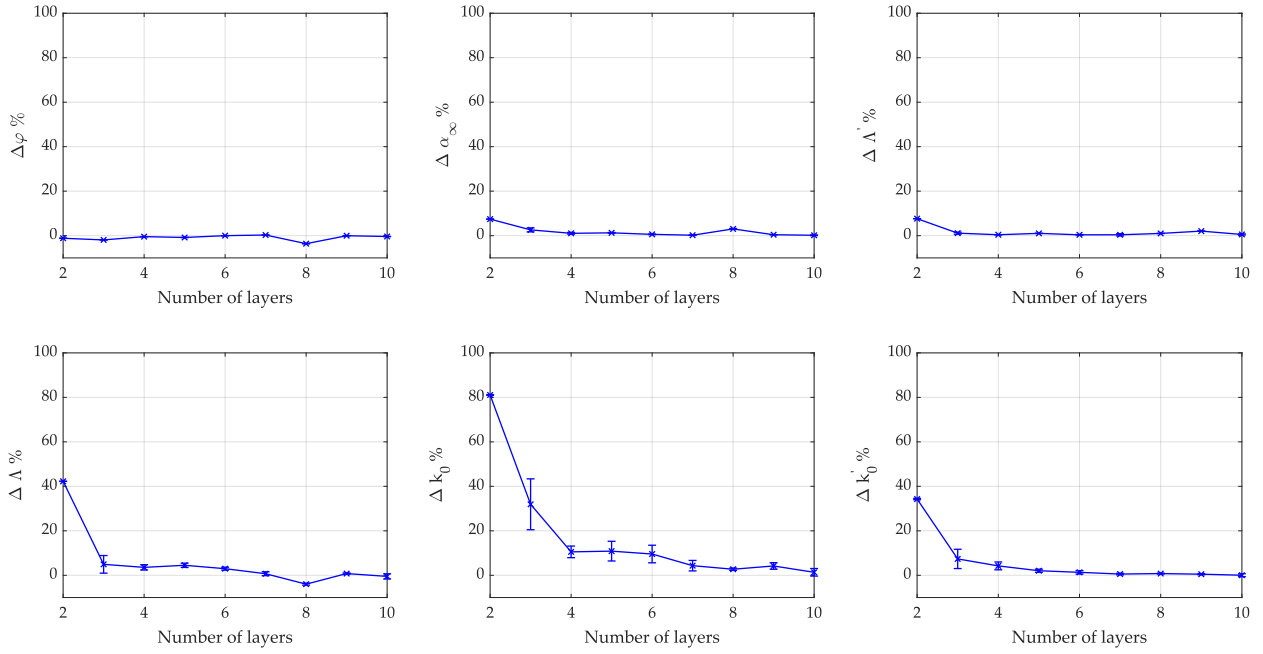
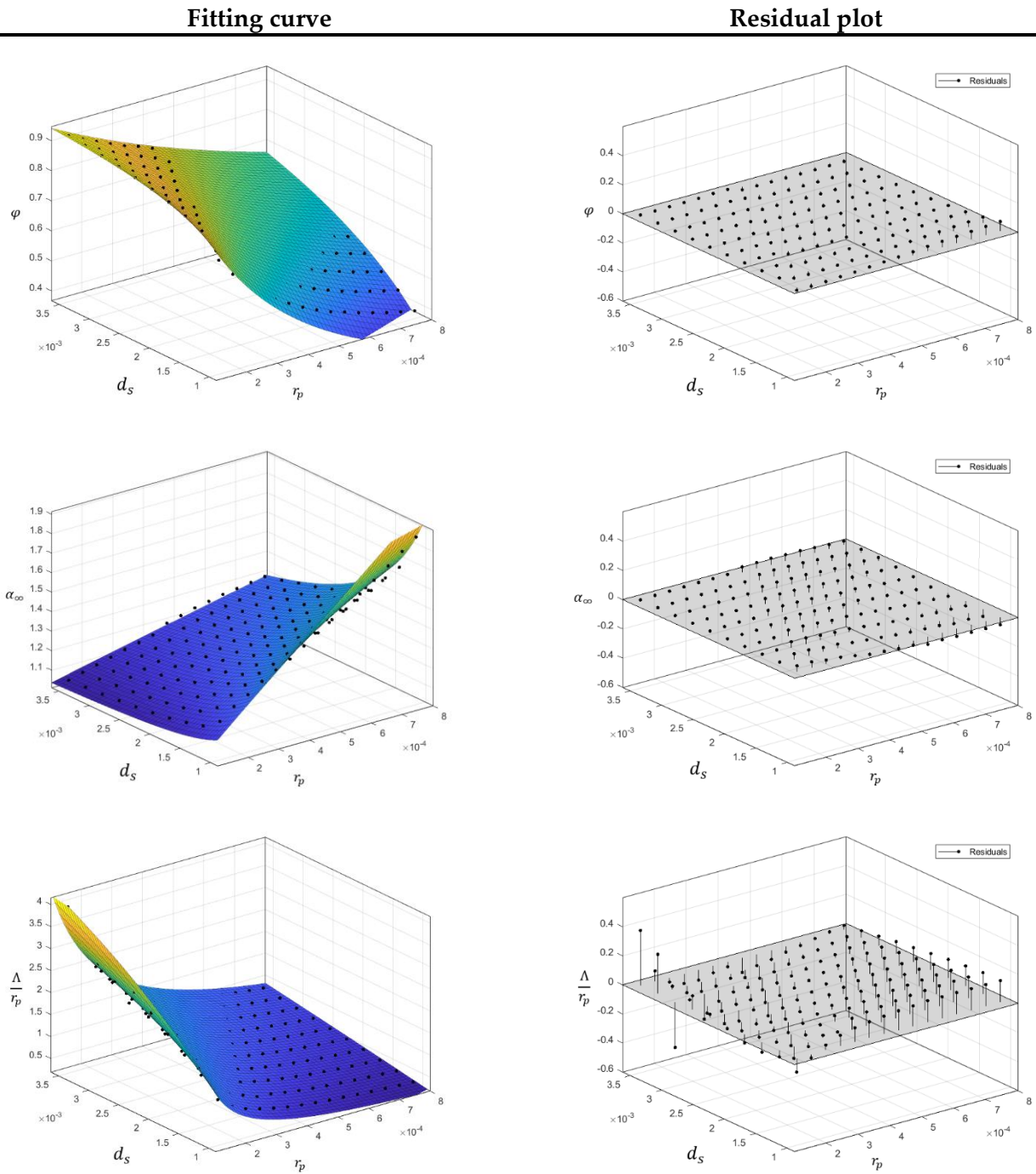


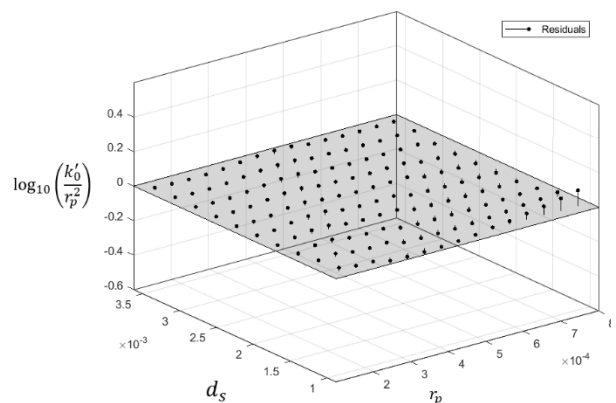
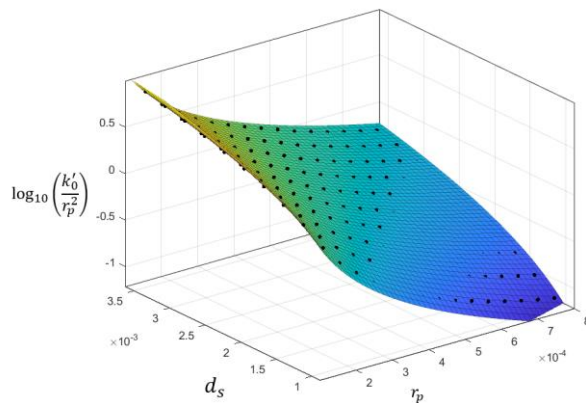
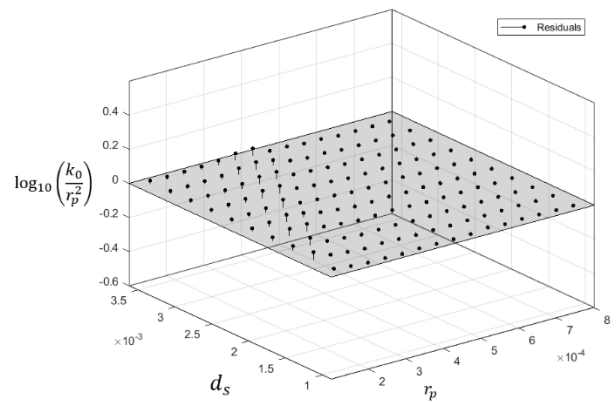
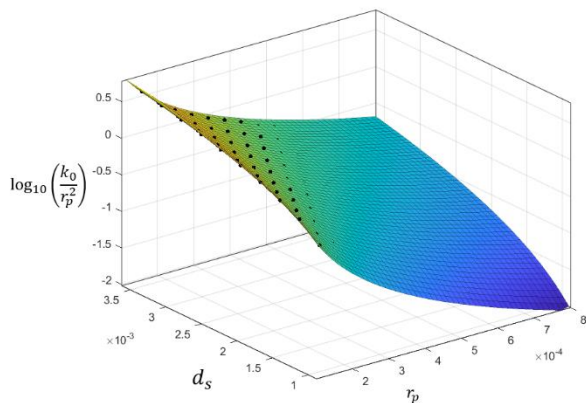
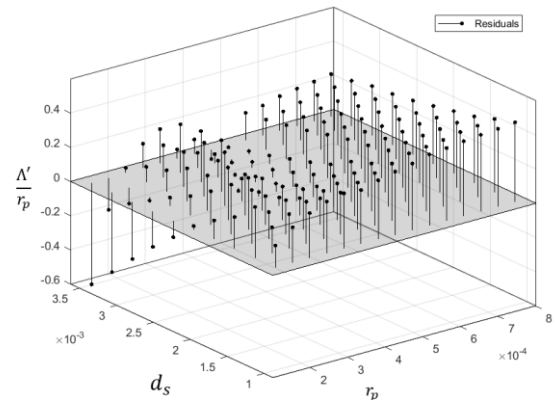
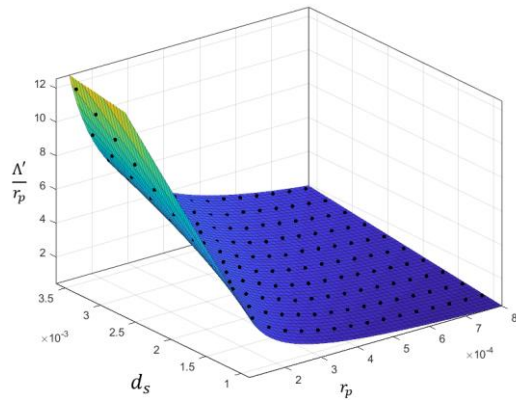
Figure 7. The relative variation between a calculation with n layers and the previous one with $n - 1$ layers for: (a) the porosity φ , (b), the high frequency limit of tortuosity α_{∞} , (c) the thermal characteristic length Λ' , (d) the viscous characteristic length Λ , (e) the static viscous permeability k_0 , (f) the static thermal permeability k'_0 .

Appendix B. Range of applicability of the transport parameter correlations.

Wire meshes are characterized by a simplicity in realization with respect to other thermoacoustic stacks. In fact, they can be derived by superimposing different layers of metal grids which are generally used for filtration applications. Therefore, the range of geometrical parameters used during numerical simulations was established based on both literature [13-14] and commercial data. The proposed correlations were summarized in Tab. I, with some statistical indicators assessing the goodness-of-fit. The coefficient of determination (R-squared) of the fit was 0.97 for the tortuosity, 0.98 for the porosity and the characteristic lengths, and 0.999 for the permeabilities. The proportionate amount of variation in the response variable (transport parameter) that is explained by the independent variables (geometrical descriptors) was therefore always very close to one. The residual analysis enables a local quantitative appreciation of the adequacy of the fitted model (Tab. IV). The residuals from a fitted model are defined as the differences between the response data (simulations) and the fitting to the response data (model) at each predictor value. The largest differences are observed for the thermal characteristic length Λ' , a strongly diverging function when $\varphi \rightarrow 1$ (see Ref. [39], Fig. 4); a behavior in agreement with the corresponding sum squared errors of residuals (SSE = 10.38, Tab. I). Together with a close match between the transport parameter values in the models and in the numerical simulations, this and the results above confirm the accuracy of the proposed correlations and indicate that they capture the essential physics of visco-thermal interactions in a wire-mesh stack.

Table IV. Fitting curve and residual plot of transport parameters correlations.





REFERENCES

- [1] C. Haddad, C. Périllon, A. Danlos, M.X. François, G. Descombes, Some Efficient Solutions to Recover Low and Medium Waste Heat: Competitiveness of the Thermoacoustic Technology, *Energy Procedia*. 50 (2014) 1056–1069. <https://doi.org/10.1016/J.EGYPRO.2014.06.125>.
- [2] G.W. Swift, Thermoacoustic engines, *J Acoust Soc Am*. 84 (1998) 1145. <https://doi.org/10.1121/1.396617>.
- [3] S. Backhaus, E. Tward, M. Petach, Traveling-wave thermoacoustic electric generator, *Appl Phys Lett*. 85 (2004) 1085–1087. <https://doi.org/10.1063/1.1781739>.

- [4] Z. Wu, L. Zhang, W. Dai, E. Luo, Investigation on a 1kW traveling-wave thermoacoustic electrical generator, *Appl Energy*. 124 (2014) 140–147. <https://doi.org/10.1016/J.APENERGY.2014.02.063>.
- [5] Z. Wu, G. Yu, L. Zhang, W. Dai, E. Luo, Development of a 3kW double-acting thermoacoustic Stirling electric generator, *Appl Energy*. 136 (2014) 866–872. <https://doi.org/10.1016/J.APENERGY.2014.04.105>.
- [6] E. Luo, W. Dai, Y. Zhang, H. Ling, Thermoacoustically driven refrigerator with double thermoacoustic-Stirling cycles, *Appl Phys Lett*. 88 (2006). <https://doi.org/10.1063/1.2176855>.
- [7] A. Piccolo, Optimization of thermoacoustic refrigerators using second law analysis, *Appl Energy*. 103 (2013) 358–367. <https://doi.org/10.1016/J.APENERGY.2012.09.044>.
- [8] I. Ramadan, H. Bailliet, G. Poignand, D. Gardner, Design, manufacturing and testing of a compact thermoacoustic refrigerator. *Applied Thermal Engineering* 2021;189:116705.
- [9] W. Dai, E. Luo, J. Hu, H. Ling, A Heat-driven thermoacoustic cooler capable of reaching liquid nitrogen temperature, *Appl Phys Lett*. 86 (2005) 1–3. <https://doi.org/10.1063/1.1941472>.
- [10] O.G. Symko, E. Abdel-Rahman, Y.S. Kwon, M. Emmi, R. Behunin, Design and development of high-frequency thermoacoustic engines for thermal management in microelectronics, *Microelectronics J*. 35 (2004) 185–191. <https://doi.org/10.1016/J.MEJO.2003.09.017>.
- [11] G. Chen, J. Xu, Development of a small-scale piezoelectric-driven thermoacoustic cooler, *Appl Therm Eng*. 213 (2022) 118667. <https://doi.org/10.1016/J.APPLTHERMALENG.2022.118667>.
- [12] E.M. Sharify, S. Hasegawa, Traveling-wave thermoacoustic refrigerator driven by a multistage traveling-wave thermoacoustic engine, *Appl Therm Eng*. 113 (2017) 791–795. <https://doi.org/10.1016/J.APPLTHERMALENG.2016.11.021>.
- [13] K. Tsuda, Y. Ueda, Critical temperature of traveling- and standing-wave thermoacoustic engines using a wet regenerator, *Appl Energy*. 196 (2017) 62–67. <https://doi.org/10.1016/J.APENERGY.2017.04.004>.
- [14] L. Liu, Y. Liu, F. Duan, Effect of the characteristic time on the system performance of a three-stage looped traveling-wave thermoacoustic engine, *Energy Convers Manag*. 224 (2020) 113367. <https://doi.org/10.1016/J.ENCONMAN.2020.113367>.
- [15] R. Yang, N. Blanc, G.Z. Ramon, Theoretical performance characteristics of a travelling-wave phase-change thermoacoustic heat pump, *Energy Convers Manag*. 254 (2022) 115202. <https://doi.org/10.1016/J.ENCONMAN.2021.115202>.

- [16] M. Hou, Z. Wu, G. Yu, J. Hu, E. Luo, A thermoacoustic Stirling electrical generator for cold exergy recovery of liquefied nature gas, *Appl Energy*. 226 (2018) 389–396. <https://doi.org/10.1016/J.APENERGY.2018.05.120>.
- [17] Q. Yang, E. Luo, W. Dai, G. Yu, Thermoacoustic model of a modified free piston Stirling engine with a thermal buffer tube, *Appl Energy*. 90 (2012) 266–270. <https://doi.org/10.1016/J.APENERGY.2011.03.028>.
- [18] G.W. Swift, W.C. Ward, Simple harmonic analysis of regenerators, *J Thermophys Heat Trans*. 10 (1996) 652–662. <https://doi.org/10.2514/3.842>.
- [19] G.W. Swift, *Thermoacoustics: a unifying perspective for some engines and refrigerators*, Springer (2018).
- [20] D.L. Johnson, J. Koplik, R. Dashen, Theory of dynamic permeability and tortuosity in fluid-saturated porous media, *J Fluid Mech*. 176 (1987) 379–402. <https://doi.org/10.1017/S0022112087000727>.
- [21] Y. Champoux, J. Allard, Dynamic tortuosity and bulk modulus in air-saturated porous media, *J Appl Phys*. 70 (1998) 1975. <https://doi.org/10.1063/1.349482>.
- [22] D. Lafarge, P. Lemarinier, J.F. Allard, V. Tarnow, Dynamic compressibility of air in porous structures at audible frequencies, *J Acoust Soc Am*. 102 (1998) 1995. <https://doi.org/10.1121/1.419690>.
- [23] M. Napolitano, R. A. Romano, R. Dragonetti, Open-cell foams for thermoacoustic applications, *Energy*. 138 (2017) 147–156. <https://doi.org/10.1016/j.energy.2017.07.042>.
- [24] E. Di Giulio, F. Auriemma, M. Napolitano, R. Dragonetti, Acoustic and thermoacoustic properties of an additive manufactured lattice structure, *J Acoust Soc Am*. 149 (2021) 3878–3888. <https://doi.org/10.1121/10.0005085>.
- [25] G. Kirchhoff, Ueber den Einfluss der Wärmeleitung in einem Gase auf die Schallbewegung, *Ann Phys*. 210 (1868) 177–193. <https://doi.org/10.1002/ANDP.18682100602>.
- [26] M.R. Stinson, The propagation of plane sound waves in narrow and wide circular tubes, and generalization to uniform tubes of arbitrary cross-sectional shape, *J Acoust Soc Am*. 89 (1998) 550. <https://doi.org/10.1121/1.400379>.
- [27] P. Morse, K. Ingard, *Theoretical acoustics*. McGraw-Hill, New York 1986.
- [28] C. Zwikker, C.W. Kosten, *Sound Absorbing Materials*. McGraw-Hill, New York, 1949.
- [29] R. Dragonetti, M. Napolitano, S. di Filippo, R. Romano, Modeling energy conversion in a tortuous stack for thermoacoustic applications, *Appl Therm Eng*. 103 (2016) 233–242. <https://doi.org/10.1016/J.APPLTHERMALENG.2016.04.076>.
- [30] W.M. Kays, A. L. London, *Compact Heat Exchangers*, McGraw-Hill, New York, 1964.

- [31] B. War, J. Clark, G. W. Swift, Design environment for low-amplitude thermoacoustic energy conversion, DELTAEC version 6.2: Users guide, Los Alamos National Laboratory, 2008.
- [32] J.L. Auriault, C. Boutin, C. Geindreau, Homogenization of Coupled Phenomena in Heterogenous Media, Homogenization of Coupled Phenomena in Heterogenous Media. (2010). <https://doi.org/10.1002/9780470612033>.
- [33] H.T. Luu, C. Perrot, V. Monchiet, R. Panneton, Three-dimensional reconstruction of a random fibrous medium: Geometry, transport, and sound absorbing properties, J Acoust Soc Am. 141 (2017) 4768–4780. <https://doi.org/10.1121/1.4989373>.
- [34] V. Langlois, A. Kaddami, O. Pitois, C. Perrot, Acoustics of monodisperse open-cell foam: An experimental and numerical parametric study, J Acoust Soc Am. 148 (2020) 1767. <https://doi.org/10.1121/10.0001995>.
- [35] M. He, C. Perrot, J. Guilleminot, P. Leroy, G. Jacqu, Multiscale prediction of acoustic properties for glass wools: Computational study and experimental validation, J Acoust Soc Am. 143 (2018) 3283. <https://doi.org/10.1121/1.5040479>.
- [36] T.G. Zieliński, R. Venegas, C. Perrot, M. Červenka, F. Chevillotte, K. Attenborough, Benchmarks for microstructure-based modelling of sound absorbing rigid-frame porous media, J Sound Vib. 483 (2020) 115441. <https://doi.org/10.1016/J.JSV.2020.115441>.
- [37] C. Perrot, G. Bonnet, M.T. Hoang, F. Chevillotte, F.-X. Bécot, L. Gautron, A. Duval, M.T. Hoang, F. Chevillotte, F.-X. Bécot, A. Duval, Microstructure, transport, and acoustic properties of open-cell foam samples, (2011) (Physical Acoustics).
- [38] R.J.S. Brown, Connection between formation factor for electrical resistivity and fluid-solid coupling factor in Biot's equations for acoustic waves in fluid-filled porous media, <Http://Dx.Doi.Org/10.1190/1.1441123>. 45 (2012) 1269–1275. <https://doi.org/10.1190/1.1441123>.
- [39] H.T. Luu, C. Perrot, R. Panneton, Influence of Porosity, Fiber Radius and Fiber Orientation on the Transport and Acoustic Properties of Random Fiber Structures, Acta Acustica United with Acustica. 103 (2017) 1050–1063. <https://doi.org/10.3813/AAA.919134>.
- [40] A. Di Meglio, E. Di Giulio, R. Dragonetti, N. Massarotti, Analysis of heat capacity ratio on porous media in oscillating flow, Int J Heat Mass Transf. 179 (2021) 121724. <https://doi.org/10.1016/J.IJHEATMASSTRANSFER.2021.121724>.
- [41] O. Doutres, Y. Salissou, N. Atalla, R. Panneton, Evaluation of the acoustic and non-acoustic properties of sound absorbing materials using a three-microphone impedance tube, Applied Acoustics. 71 (2010) 506–509. <https://doi.org/10.1016/J.APACOUST.2010.01.007>.

- [42] B.H. Song, J.S. Bolton, A transfer-matrix approach for estimating the characteristic impedance and wave numbers of limp and rigid porous materials, *J Acoust Soc Am.* 107 (2000) 1131. <https://doi.org/10.1121/1.428404>.
- [43] A. Petculescu, L.A. Wilen, Lumped-element technique for the measurement of complex density, *J Acoust Soc Am.* 110 (2001) 1950. <https://doi.org/10.1121/1.1401743>.
- [44] L.A. Wilen, Dynamic measurements of the thermal dissipation function of reticulated vitreous carbon, *J Acoust Soc Am.* 109 (2001) 179. <https://doi.org/10.1121/1.1333422>.
- [45] M. Napolitano, E. Di Giulio, F. Auriemma, R.A. Romano, R. Dragonetti, Low frequency acoustic method to measure the complex bulk modulus of porous materials, *J Acoust Soc Am.* 151 (2022) 1545. <https://doi.org/10.1121/10.0009767>.
- [46] E. Di Giulio, M. Napolitano, A. Di Meglio, R.A. Romano, R. Dragonetti, Low frequency acoustic method to measure the complex density of porous materials, *J Acoust Soc Am.* 152 (2022) 2220. <https://doi.org/10.1121/10.0014762>.